Article

First Experiment of Spin Contrast Variation Small-Angle Neutron Scattering on the iMATERIA Instrument at J-PARC

Yohei Noda [1,*], Tomoki Maeda [1] , Takayuki Oku [1,2] , Satoshi Koizumi [1,*], Tomomi Masui [3] and Hiroyuki Kishimoto [3]

[1]   Institute of Quantum Beam Science, Ibaraki University, 162-1 Shirakata, Tokaimura, Nakagun, Ibaraki 319-1106, Japan; tomoki.maeda.polymer@vc.ibaraki.ac.jp (T.M.); takayuki.oku@j-parc.jp (T.O.)
[2]   J-PARC Center, Japan Atomic Energy Agency, 2-4 Shirakata, Tokaimura, Nakagun, Ibaraki 319-1106, Japan
[3]   Sumitomo Rubber Industries, Ltd., 1-1-2 Tsutsuicho, Chuoku, Kobe 651-0071, Japan; t-masui.az@srigroup.co.jp (T.M.); h-kishimoto.az@srigroup.co.jp (H.K.)
*   Correspondence: yohei.noda.77@vc.ibaraki.ac.jp (Y.N.); satoshi.koizumi.prof@vc.ibaraki.ac.jp (S.K.); Tel.: +81-29-352-3243 (Y.N.); Tel.: +81-29-352-3245 (S.K.)

check for updates

Abstract: Recently, we have developed a novel dynamic nuclear polarization (DNP) apparatus with a magnetic field of 7 T and a sample temperature of 1 K. High proton spin polarizations from -84% to 76%, for TEMPO doped polystyrene samples, have been demonstrated. This DNP apparatus satisfies the simultaneous requirement for quick and easy sample exchange and high DNP performance. On the iMATERIA (BL20) instrument at J-PARC, the first beam experiment using this DNP apparatus has been performed. For this experiment, the beamline was equipped with a supermirror polarizer. The stray magnetic field due to the superconducting magnet for DNP was also evaluated. The stray magnetic field plays an important role for in maintaining the neutron polarization during the transportation from the polarizer to the sample. The small-angle neutron scattering (SANS) profiles of silica-filled rubber under dynamically polarized conditions are presented. By applying our new analytical approach for SANS coherent scattering intensity, neutron polarization (P_N) as a function of neutron wavelength was determined. Consequently, for the neutron wavelength, range from 4 Å to 10 Å, $|P_N|$ was sufficient for DNP-SANS studies.

Keywords: small-angle neutron scattering; contrast variation; dynamic nuclear polarization; J-PARC

1. Introduction

A key advantage of small-angle neutron scattering (SANS), is that we can vary the contrast without changing the structural properties of the sample. Contrast variation is very effective for studies of multi-component systems. The neutron coherent scattering lengths of deuterium and proton are very different and opposite in sign. So, deuterium substitution is very effective for contrast variation. There are many applications to solution, gel and biological systems with great success. Here, low-cost deuterated solvents are often useful. However, deuteration of the polymers themselves is often very expensive, and we believe that an alternative contrast-variation technique will be of great benefit for polymer studies.

Neutrons have a spin, and the protons in a sample also have a spin. Between the parallel and anti-parallel spin configurations, the neutron coherent scattering length is very different. This effect can also be used for contrast variation, and we have focused on this proton spin polarization approach.

At room temperature and in a weak magnetic field, almost equal numbers of up and down proton spins are randomly populated. To "polarize" means to align the spins in one particular direction,

and the "polarization" is defined as the difference of up and down spin populations. In thermal equilibrium, the polarization increases with increasing Zeeman splitting energy by increasing magnetic field and lowering temperature. However, even at 6.7 T and 1.2 K, polarization of a proton (P_H) is only 0.57%. On the other hand, electron spin polarization is almost fully polarized at the same condition. By microwave irradiation, "polarization transfer" occurs, and high proton spin polarizations can be achieved. This is called "dynamic nuclear polarization", or DNP. There are four essential conditions; electron spin doping, magnetic field, low temperature, and microwave irradiation [1,2].

The first experimental hurdle is how to introduce electron spins into a sample. The stable radical 2,2,6,6-tetramethylpiperidine 1-oxyl (TEMPO) is known to show a good polarizing performance. In addition, TEMPO is volatile around room temperature, and vaporized TEMPO molecules spontaneously permeate the fluid phase of polymers. This phenomenon can be utilized for electron spin doping (vapor sorption technique [3]). Since the optimum concentration for DNP is quite low (50 mM), effect on micro-domain structure is negligible. In contrast to deuterium substitution, this is a "post-synthesis treatment", directly applicable to real industrial products. By use of this technique, we have performed DNP-SANS studies for polyethylene [4], block copolymer [5], and rubber composite materials [6].

In Figure 1a, the history of DNP-SANS instruments is summarized. In 1986, the pioneering work of DNP-SANS was first performed by Stuhrmann et al. [7]. They used a ^{3}He-^{4}He dilution refrigerator to achieve very low temperatures (0.3 K) and high polarization of $P_H = 80\%$. In 1987, Masuda at KEK developed a DNP-SANS instrument based on a ^{3}He evacuation cryostat (0.5 K) [8]. However, these highly specialized setups have not become widespread as a routine research tool. Later, in 2004, van den Brandt at PSI developed a ^{4}He evacuation cryostat type instrument [9]. The sample conditions were 3.5 T and 1 K. The polarization P_H was limited to below 40%, but this simple and quick setup is excellent for SANS study. Our former setup employed the same approach [4–6,10].
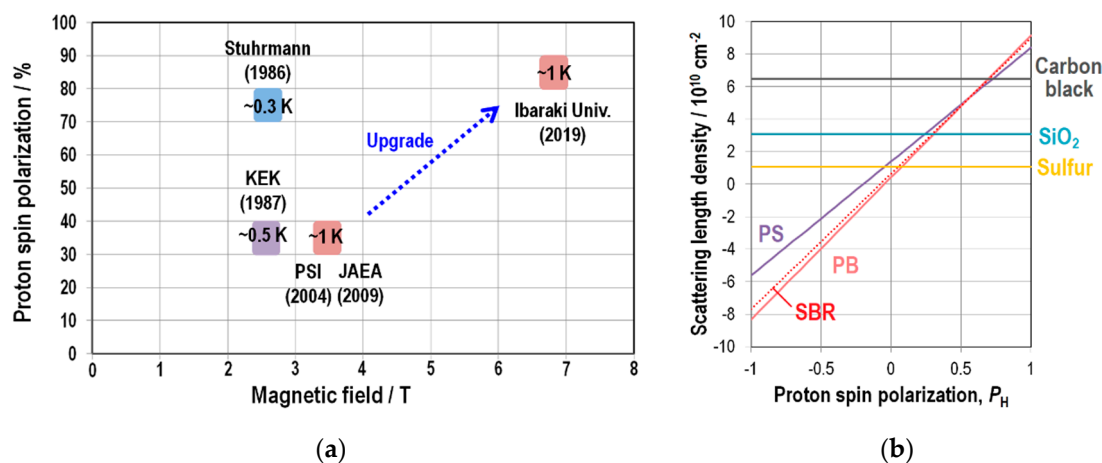

Figure 1. (**a**) Upgrade history of dynamic nuclear polarization-small-angle neutron scattering (DNP-SANS) instruments. (**b**) P_H dependence of scattering length density of typical rubber composite. P_N is assumed to be 1.

Figure 1b shows neutron scattering length density (SLD) of typical rubber composites, (styrene-butadiene random copolymer (SBR), polystyrene (PS), polybutadiene (PB), sulfur, silica, zinc oxide, and carbon) as a function of proton spin polarization, P_H. Only the SBR component includes hydrogen. So, its scattering length density changes significantly. In our former setup, polarization performance was limited (≤40%), and this was sufficient to match the SLD of SBR with that of silica. However, a higher P_H of ~70% is necessary to contrast match between SBR and carbon.

In order to achieve higher P_H, we have developed a new DNP apparatus with a magnetic field of 7 T. The necessary microwave frequency is proportional to the magnetic field, and we obtained 188 GHz by use of 94 GHz source and a frequency doubler. Thanks to progress in microwave technology in the

30 years since Struhrmann's pioneering work, compact and highly efficient diode-type devices are now commercially available.

Recently, we have developed DNP apparatus with magnetic field 7 T and low temperature 1 K [11]. We have achieved high P_H performance (from −84% to 76%) for TEMPO-doped polystyrene samples. This DNP apparatus satisfies the requirement for quick and easy sample exchange and high DNP performance, at the same time. In this article, we report the first beam experiment using this DNP apparatus conducted on iMATERIA (BL20) [12] at J-PARC's Materials and Life Science Facility (MLF) [13–15]. In the course of the experiment, the beamline was equipped with neutron polarizing devices: we describe the design and performance of the newly installed supermirror polarizer and give an evaluation of the stray magnetic field generated by superconducting magnet. For maintaining neutron polarization during the transportation from the supermirror polarizer to the sample position, a guide magnetic field is necessary. In addition, it is difficult for supermirror polarizer to polarize short wavelength neutrons, since the critical angle is proportional to the neutron wavelength. Hence, in DNP-SANS studies, care must be taken in selecting a neutron wavelength range which keeps $|P_N|$ is high. Finally, we describe the result of a DNP-SANS experiment for silica-filled rubber, and we suggest a new P_N determination approach using coherent small-angle neutron scattering.

2. Experiment

2.1. DNP Apparatus

Our DNP apparatus is composed of a super-conducting magnet (7 T), ^{4}He-evacuation-cryostat-type sample chamber (1 K), an NMR circuit (288 MHz) and a microwave unit (188 GHz). The detail of the setup has already been reported [11]. Here, we describe the features relating to SANS measurement. Figure 2a shows a sectional view. A sample is loaded from the top and immersed in liquid He. Thin aluminum windows are used for the neutron beam path. Figure 2c shows the sample stick. The neutron beam is collimated by a 10 mm diameter cadmium pinhole placed just in front of the sample. A sample is set into this teflon part and surrounded by the NMR coil for P_H evaluation. The sample is typically a self-standing sheet. (area 14 mm × 14 mm, ca. 1 mm thickness). In order to minimize the SANS background, the NMR coil is made of thin aluminum plate (0.3 mm thick).
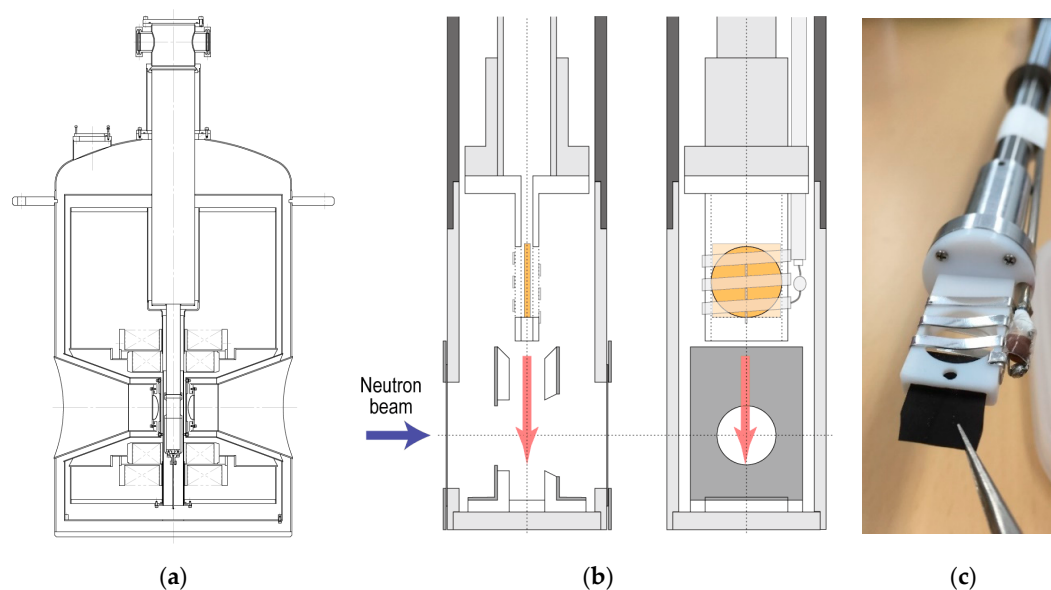

(**a**)   (**b**)   (**c**)

Figure 2. Sample environment: (**a**) Section view of super-conducting magnet; (**b**) Schematic view of sample-stick end (the red arrows indicate the way of sample insertion); (**c**) Photograph of sample-stick end during the insertion of rubber sheet sample.

2.2. SANS Instrument (BL20 iMATERIA)

Figure 3 shows a schematic of iMATERIA at J-PARC. The pulsed neutron beam (wavelength from 1 Å to 10 Å at double frame operation) illuminates the sample. The scattered neutrons are then detected by position-sensitive detectors (PSDs) filled with ^{3}He gas. The PSDs are classified into the 4 banks: small-angle (SA), low-angle (LA), sample environment (SE) and back-scattering (BS) detector banks. The DNP apparatus limits the scattering angle (2θ) less than 20° to the forward and backward directions. In this study, we will use the SA bank and a part of LA bank. In the future, we plan to use the BS bank for measuring diffraction peaks to determine crystallographic structures. For minimizing scattering by air, the sample space is surrounded by a vacuum chamber. The DNP apparatus has a flange on its side, which compatible with iMATERIA's vacuum chamber.
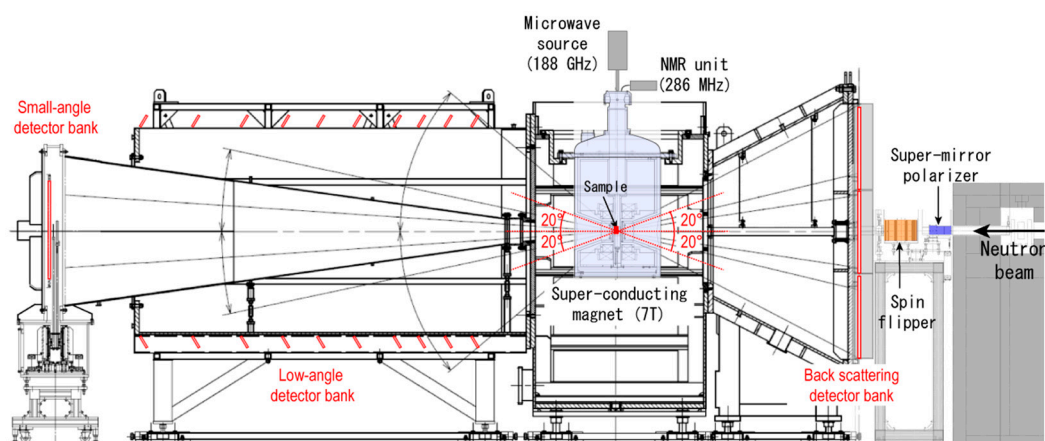

Figure 3. DNP-SANS experiment layout at iMATERIA.

2.3. Stray Magnetic Field

When applying the 7 T magnetic field at the sample position, the superconducting magnet generates stray magnetic field in the surrounding space. The exposure threshold, for the public, is limited to 0.5 mT, according to ICNIRP guidelines [16], and we must, therefore, restrict public access in the areas with magnetic field higher than 0.5 mT, in order to prevent interference with implanted artificial cardiac pacemakers.

According to the simple electromagnetic calculation assuming no surrounding magnetic substances, the 0.5 mT stray magnetic field distance from the magnet center was evaluated to be 4.88 m or 3.85 m to the coil axis or the perpendicular direction, respectively, as shown by the dotted purple lines in Figure 4. However, the stray magnetic field is strongly affected by magnetic substances. The vacuum chamber of iMATERIA is composed of non-magnetic metals (stainless steel, SUS304 and aluminum). However, general structural steel (SS400) is used for the supporting frame of the vacuum chamber and the surrounding radiation-shielding blocks. The stray magnetic field, considering the surrounding magnetic substances, was calculated by use of electromagnetic finite-element analysis software (Ansys Maxwell, Ansys). Figure 4 shows the calculated magnetic field distribution around iMATERIA at 7 T. The solid purple contour line indicates the position at which the magnetic field is 0.5 mT.

By considering the surrounding steel, the calculated magnetic field is decreased, shrinking the 0.5 mT line inward. Fortunately, the majority of 0.5 mT area is calculated to be within the shield room of iMATERIA or inaccessible areas. The upstream side of the shield room (the right side on top view in Figure 4) is occupied by the shield room for neutron beam guide tubes. The BL19 side is also occupied by the shield room for BL19 neutron beam guide. Only the BL21 side is human-accessible, and the magnetic field is higher than 0.5 mT, just in front of the door of the shield room. There, a warning sign is necessary. In addition, at the passage shown in the side view of Figure 4, the magnetic field is

calculated to be less than 0.5 mT. The calculated results were confirmed to be correct by use of a 3-axis Hall magnetometer (THM1176, Metrolab).
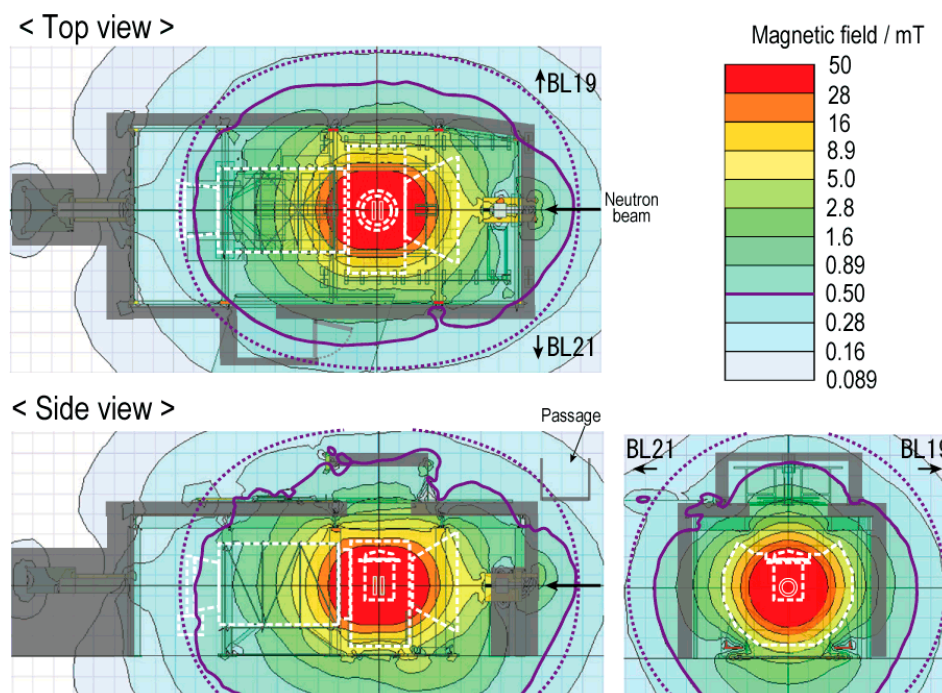

Figure 4. Calculated stray magnetic field taking account of surrounding magnetic materials, when energizing the superconducting magnet up to 7 T. The solid and dotted purple lines indicate the 0.5 mT contour, with and without considering surrounding magnetic substances, respectively. The dashed white line shows the iMATERIA vacuum chamber and the super-conducting magnet. The dark gray area indicates the wall of the shield room of iMATERIA. BL19 and BL21 refer to the neighboring instruments.

2.4. Supermirror Polarizer

In order to polarize the incident neutron beam, we installed a transmission-type Fe/Si supermirror polarizer, from Avance (Japanese agent of Swiss Neutronics). As shown in Figure 5, sixteen plates of supermirror are placed in a zig-zag arrangement (so-called V-cavity [17,18]). Neutrons with spin up are selectively reflected out of the beam, to generate a transmitted beam with spin down. Therefore, the sign of neutron polarization is negative as we will see later. Each supermirror plate is a 0.3 mm-thick Si substrate, both sides of which are coated with an $m = 5$ supermirror coating (Fe/Si) (here, m indicates a factor of the critical angle for neutron reflection in relation to nickel). By employing the V-cavity arrangement, the supermirror is very short (18 cm) along the neutron beam direction. This is significantly advantageous since there is only a limited space for new devices on the upstream side of the vacuum chamber (60 cm along the neutron beam direction). The supermirror covers a 25×25 mm^2 neutron beam. In normal SANS experiments, a neutron beam with the cross section of 20×20 mm^2 is collimated at this position. The supermirror was surrounded by a magnetic housing made by steel and permanent magnets, in order to generate 45 mT and saturate the magnetization of the supermirror. According to the manufacturer's specification sheet (Swiss Neutronics), the neutron polarization is 98.0%, for a neutron wavelength of 5 Å.
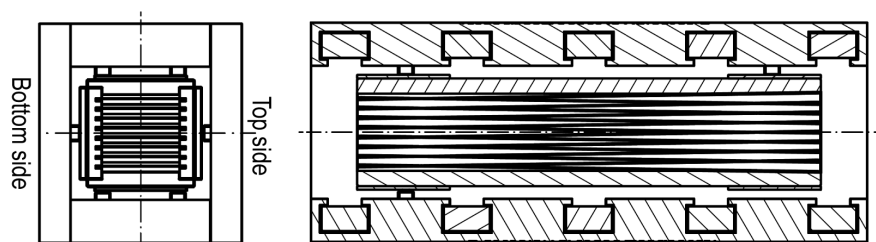
Figure 5. Schematic view of supermirror polarizer.

The magnetic field due to superconducting magnet at the neutron polarizer (2.5 m upstream of the center of the superconducting magnet), was measured to be 4.7 mT (significantly higher than Earth's field), and we used this stray magnetic field to transport the polarized neutron beam without depolarization.

2.5. Sample Preparation

We studied a silica-filled rubber sample, whose composition is shown in Table 1. As a polarizing agent, the stable free radical TEMPO was introduced into the 0.0494 cm-thick rubber sample by vapor permeation (40 °C for 1 week). In order to avoid absorption of O_2 by the sample, we employed a vacuum glove box (UNICO-1000Ls-INRS, UNICO) with a gas-purification system (MF-100, UNICO). The oxygen content around the sample was maintained below 1 ppm. The TEMPO concentration was determined to be 40.9 mM by ESR measurement (SPINSCAN, ADANI), and close to the known optimum concentration (50 mM) for DNP at 7 T.

Table 1. Sample composition.

Component	SBR	Silica	Plasticizer Oil	Silane-Coupling Agent	Organic Accelerators	Sulfur
Volume fraction/%	64.7	15.5	15.1	2.3	1.8	0.46

3. Results and Discussion

3.1. NMR Determination of P_H

For evaluating P_H, continuous wave NMR was used. As shown in Figure 6a, the small NMR signal in thermal equilibrium (TE) significantly increased by several hundred times after applying microwaves. For lower and higher microwave frequencies, the NMR signal was positively and negatively enhanced, respectively. From the enhancement factors, P_H values were calculated to be +72.2% and −63.2%. The microwave frequency was modulated with a modulation amplitude of 0.18 GHz and a modulation frequency of 10 kHz. Otherwise, $|P_H|$ becomes much lower.
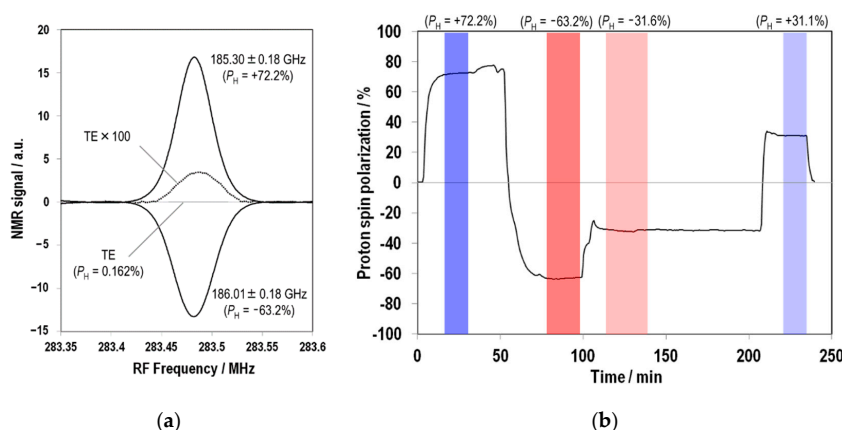
Figure 6. Proton spin polarization measurements: (**a**) Proton NMR signal before and after the microwave irradiation for DNP; (**b**) Time profile of proton spin polarization for the SANS experiment.

In our previous study [11], TEMPO-doped polystyrene indicated high $|P_H|$ at 6.7 T with applying frequency-modulated microwave. "Thermal mixing" is known to be a dominant DNP mechanism for TEMPO-doped samples at 1 K and several T [1,2]. In the thermal mixing mechanism, a spectral diffusion over the inhomogeneously broadened spin packets plays an important role for achieving high $|P_H|$. Our previous study of TEMPO-doped polystyrene sample indicated that magnetic field increase from 3.35 T to 6.7 T deteriorated $|P_H|$ but significantly recovered by microwave frequency modulation. This can be understood as follows: The magnetic field increase weakens the coupling between the neighboring spin packets to inactivate spectral diffusion. The microwave frequency modulation compensates this inactivation. This microwave frequency modulation approach at high magnetic field was proved to be effective also for the silica-filled rubber sample.

Figure 6b shows the time profile of P_H for the actual SANS experiment. By applying microwaves and tuning the frequency, we have achieved high positive polarization. The polarization build-up took about 15 min to reach its maximum, and full inversion of P_H took 30 min. The color bars indicate the periods of the SANS measurement described below.

3.2. SANS Profile under DNP Condition

Figure 7 shows the SANS profiles observed at various values of P_H. The horizontal axis is the magnitude of the scattering vector, q (=$(4\pi/\lambda)\sin\theta$, here, λ is the neutron wavelength, and 2θ is the scattering angle.) The low-q side profiles were obtained by the SA detector bank ($0.6° < 2\theta < 5.5°$) and the high-q side profiles were obtained by the LA detector bank ($12° < 2\theta < 40°$). Figure 3 shows the positions of the detector banks. However, scattered neutrons with $2\theta > 20°$ were shielded by the neutron beam window of the superconducting magnet. The small gap between the low-q and high-q side profiles was due to the gap in 2θ between the SA and LA banks, mentioned above, and the limited neutron wavelength range (from 4 Å to 10 Å). Although the full range is from 1 Å to 10 Å for iMATERIA in double frame mode, the neutron polarization decreases significantly at the shorter wavelengths, as shown later.

On the low-q side, the coherent scattering contribution due to the contrast between silica particles and SBR rubber matrix is dominant. In this low-q region, we observe the minimum scattering intensity at $P_H = -31\%$, around which the SLD of silica particles matches that of SBR rubber matrix. Figure 1b shows the SLDs as a function of P_H: please note that P_N is negative at the present experiment. Since the coherent scattering contribution, which is proportional to silica particle's form factor, deteriorates at higher-q, the incoherent scattering contribution dominates on the high-q side. In this region, the scattering intensity increases monotonically with increasing P_H, as shown later in detail (Section 3.4).
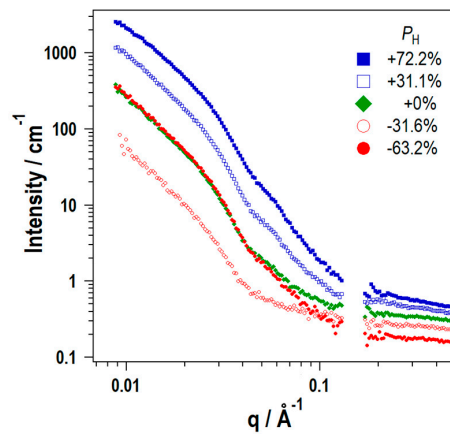
Figure 7. SANS profiles with limited neutron wavelength from 4 Å to 10 Å, for the silica-filled rubber at various P_H.

3.3. P_H Dependence of Neutron Transmission

The neutron transmission, T is given by the following equation.

$$T = \exp[-\sum\nolimits_{tot} d_s]. \tag{1}$$

Here, $\sum_{tot}$ is a total macroscopic cross section and d_s is a sample thickness.

$$\sum\nolimits_{tot} = \sum\nolimits_i n_i \sigma_{i,tot}. \tag{2}$$

Here, n_i and $\sigma_{i,tot}$ are the number density and the total cross section of the nuclear species "i". By use of the chemical composition of the sample and the known total cross section for each nucleus ($\sigma_{H,tot} = (81.99 - 67.00 P_H P_N) \times 10^{-24}$ cm^2, $\sigma_{C,tot} = 5.55 \times 10^{-24}$ cm^2, $\sigma_{N,tot} = 13.41 \times 10^{-24}$ cm^2, $\sigma_{O,tot} = 4.23 \times 10^{-24}$ cm^2, $\sigma_{Si,tot} = 2.34 \times 10^{-24}$ cm^2, $\sigma_{S,tot} = 1.56 \times 10^{-24}$ cm^2 [19]), we obtained that $\sum_{tot} = (4.51 - 3.50 \, P_H \, P_N)$ cm^{-1}. In Figure 8a, the black circles indicate the experimentally obtained T as a function of P_H. They agree well with numerical calculation using Equation (1).
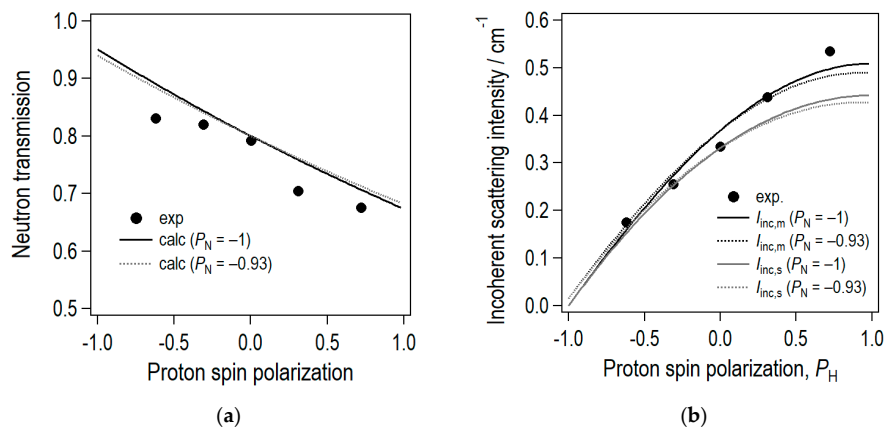

(a)

(b)

Figure 8. (**a**) Neutron transmission as a function of proton spin polarization. The black circles indicate experimentally obtained average values for the neutron wavelengths between 4 Å and 6 Å. The solid and dotted lines are numerically calculated for $P_N = -1$ and -0.93, respectively. (**b**) Incoherent scattering intensity as a function of proton spin polarization. The black and gray lines indicate numerically calculated incoherent scattering intensity with and without considering multiple scattering, respectively. The solid and dotted lines are numerically calculated for $P_N = -1$ and -0.93, respectively.

3.4. P_H Dependence of Incoherent Scattering Intensity

The incoherent scattering intensity ($I_{inc,s}$) is given by the following equation.

$$I_{inc,s} = \sum{}_{inc}/(4\pi). \tag{3}$$

Here, $\sum_{inc}$ is a macroscopic incoherent scattering cross section [cm^{-1}].

$$\sum{}_{inc} = \sum{}_i n_i \sigma_{i,inc}. \tag{4}$$

Here, $\sigma_{i,inc}$ is the incoherent scattering cross section of the nuclear species "i". By use of the chemical composition of the sample and the known incoherent cross section data for each nucleus ($\sigma_{H,inc} = 79.92\ (1 - (2/3)P_H P_N - (1/3)P_H{}^2) \times 10^{-24}$ cm^2, $\sigma_{C,inc} = 0.001 \times 10^{-24}$ cm^2, $\sigma_{N,inc} = 0.5 \times 10^{-24}$ cm^2, $\sigma_{O,inc} = 0.004 \times 10^{-24}$ cm^2, $\sigma_{Si,inc} = 0.007 \times 10^{-24}$ cm^2, $\sigma_{S,inc} = 1.56 \times 10^{-24}$ cm^2 [19]), we obtain that $\sum_{inc} = 4.17\ (1 - (2/3)P_H P_N - (1/3)P_H{}^2)$ cm^{-1}. The contribution to $\sum_{inc}$ due to nuclei other than protons was negligible (0.001 cm^{-1}).

According to the literature [20], the incoherent scattering intensity, $I_{inc,m}$ with consideration of multiple scattering is given by the following equation.

$$I_{inc,m} = \exp(\sum{}_{inc} d_s - 1)/(4\pi d_s). \tag{5}$$

Figure 8b shows the observed scattering intensity at high-q (q = 0.3–0.4 Å^{-1}) and the calculated $I_{inc,s}$ and $I_{inc,m}$ with P_N = −0.93 and −1. The observed high-q intensity agrees well with the calculated $I_{inc,m}$. However, at P_H = +0.72, the observed high-q intensity was slightly higher than the calculated $I_{inc,m}$. This excess scattering, beyond the incoherent scattering, is likely due to local structure within the matrix domain. For this P_H, $b_{H,coh}$ is significantly negative and much different from the scattering lengths of other nuclei.

3.5. P_H Dependence of Coherent Scattering Intensity and Detemination of P_N

For precise analysis of contrast variation experiment, one needs to determine the correct value of P_N. Short-wavelength neutrons are difficult to polarize because of their shallow critical reflection angle. So, we need to evaluate the P_N as a function of neutron wavelength.

In iMATERIA, neutron scattering experiments with a wide wavelength range (1 Å–10 Å) can be conducted in double-frame mode. By use of time-of-flight (TOF) approach we can separate neutrons with different wavelengths. The position and time of each neutron detection event were registered in "event-mode" format. We can then re-analyze the scattering data with a selected neutron wavelength range afterwards.

The coherent scattering intensity of 2-component system is proportional to the contrast factor ($\Delta\rho^2$) which is defined as the difference of SLD between two domains A and B as follows.

$$\Delta\rho^2 = (\rho_A - \rho_B)^2. \tag{6}$$

Here, ρ_A and ρ_B are the scattering length densities of domains A and B.

$$\begin{aligned}\rho_A &= \sum{}_i n_{iA} b_{i,coh}, \\ \rho_B &= \sum{}_i n_{iB} b_{i,coh}.\end{aligned} \tag{7}$$

Here, $n_{i,A}$ and $n_{i,B}$ are the number density of the nuclear species "i" at the domains A and B, respectively. $b_{i,coh}$ is the coherent scattering length of the nuclear species "i". The coherent scattering length of proton ($b_{H,coh}$) is given by the following equation:

$$b_{H,coh} = b_0 + b_N \boldsymbol{\sigma} \bullet \mathbf{I}, \tag{8}$$

here, $b_0 = -0.374 \times 10^{-12}$ cm, $b_N = 5.824 \times 10^{-12}$ cm, and σ and I are quantum mechanical operators for neutron and proton spins, respetively [21]. The expectation values for $b_{H,coh}$ and $b_{H,coh}{}^2$ are calculated as follows.

$$<b_{H,coh}> = b_0 + (1/2)b_N P_N P_H, \tag{9}$$

$$<b_{H,coh}{}^2> = b_0{}^2 + (1/2)b_0 b_N P_N P_H + (1/4)(b_N/2)^2 P_H{}^2. \tag{10}$$

If $|P_N| = 1$, $<b_{H,coh}>^2 = <b_{H,coh}{}^2>$ is always satisfied. However, if $|P_N| < 1$, we should notice that $<b_{H,coh}>^2 \neq <b_{H,coh}{}^2>$. Then, we calculate the SLD of domains A and B as follows.

$$\rho_A = \rho_A' + n_{H,A} b_{H,coh}, \tag{11}$$

$$\rho_B = \rho_B' + n_{H,B} b_{H,coh}. \tag{12}$$

Here, in each equation, the first term (ρ_A' and ρ_B') is due to nuclei other than protons, and the second term ($n_{H,A} b_{H,coh}$ and $n_{H,B} b_{H,coh}$) is the contribution only due to protons. $n_{H,A}$ and $n_{H,B}$ indicate the number densities of protons in components A and B, respectively. Applying Equations (1) and (8), and parameter substitution, the following equations are obtained:

$$\rho_A = \alpha_A + 2\beta_A \sigma \bullet I, \tag{13}$$
$$\rho_B = \alpha_B + 2\beta_B \sigma \bullet I. \tag{14}$$

Here, α_A ($= \rho_A' + n_{H,A} b_0$) and α_B ($= \rho_B' + n_{H,B} b_0$) are the scattering length densities for the case with $P_H = 0$. On the other hand, β_A ($= n_{H,A} b_N/2$) and β_B ($= n_{H,B} b_N/2$) are the proportionality constants for the polarization-dependent term. Then, the expectation value of the contrast factor is calculated as follows:

$$<\Delta\rho^2> = <(\alpha_A - \alpha_B)^2 + 4(\alpha_A - \alpha_B)(\beta_A - \beta_B)\sigma \bullet I + 4(\beta_A - \beta_B)^2(\sigma \bullet I)^2>,$$
$$= (\alpha_A - \alpha_B)^2 + 2(\alpha_A - \alpha_B)(\beta_A - \beta_B)P_N P_H + (\beta_A - \beta_B)^2 P_H{}^2. \tag{15}$$

The contrast factor is a quadratic function as a function of P_H. If $P_N = 1$, $<\Delta\rho^2> = [(\alpha_A + \beta_A P_H) - (\alpha_B + \beta_B P_H)]^2$. The contrast factor has a local minimum when P_H satisfies $(\alpha_A + \beta_A P_H) = (\alpha_B + \beta_B P_H)$ (so called "matching point between domain A and B"). On the other hand, if $P_N = 0$, $<\Delta\rho^2> = (\alpha_A - \alpha_B)^2 + (\beta_A - \beta_B)^2 P_H{}^2$. The local minimum value $((\alpha_A - \alpha_B)^2)$ is positioned at $P_H = 0$. In this way, the P_H dependence of the contrast factor is sensitively affected by P_N. This can be utilized for P_N determination as shown below.

We observed the SANS intensity as a function of P_H experimentally. The SANS intensity is composed of both coherent and incoherent scattering terms. After subtracting the incoherent scattering, we obtain the coherent scattering intensity ($I_{coh}(P_H)$), which is proportional to the contrast factor if the sample is a 2-component system. By least-squares fitting of $I_{coh}(P_H)$ to the quadratic function as follows, the parameters K, L, and M can be determined.

$$I_{coh}(P_H) = K + L P_H + M P_H{}^2. \tag{16}$$

Since $I_{coh}(P_H)$ is proportional to $<\Delta\rho^2>$, the following equations are obtained.

$$K = c(\alpha_A - \alpha_B)^2, \tag{17}$$

$$L = 2c(\alpha_A - \alpha_B)(\beta_A - \beta_B)P_N, \tag{18}$$

$$M = c(\beta_A - \beta_B)^2. \tag{19}$$

Here, c is a constant. Therefore, we obtain the following equation.

$$|P_N| = L/(4KM)^{1/2}. \tag{20}$$

An advantage of this approach is that the only assumption we need is that the sample should be composed of two components. The detailed chemical composition and the densities of each component do not affect the result.

This approach was applied to the SANS data as follows. We used Equation (5) to calculate I_{inc}, which depends on P_H and P_N. We scanned P_N to find a self-consistent value of P_N, which is closest to P_N calculated by Equation (20). Fortunately, in the low-q side, the coherent scattering contribution is much larger than the incoherent scattering contribution. In many cases, the difference of input P_N caused only a slight effect on the P_N calculated by Equation (20).

We calculated scattering intensity difference as a function of P_H, for each neutron wavelength contribution. Using Equations (5) and (20), the self-consistent $|P_N|$ was calculated as shown in Figure 9b. We obtained that $|P_N| = 0.93 \pm 0.01$ for neutron wavelength from 4 Å to 10 Å. The evaluated $|P_N|$ is slightly lower than the value from the Swiss Neutronics specification sheet. This is because the beam divergence in iMATERIA is greater than that in the manufacturer's setup.
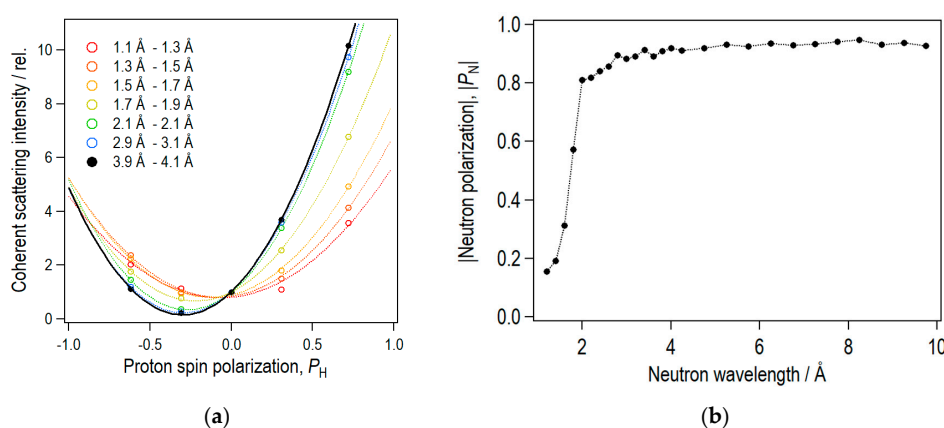

(a)　　　　　　　　　　　　　　　　(b)

Figure 9. (**a**) Coherent scattering intensity as a function of P_H. (**b**) Evaluated neutron spin polarization, $|P_N|$ as a function of neutron wavelength.

4. Conclusions

By use of 7 T DNP apparatus, the first DNP-SANS experiment was performed successfully. We successfully introduced neutron polarizing devices. This is the world's first DNP-SANS instrument realizing quick sample exchange and high polarization performance at the same time. This instrument is now open for users under industry-user program run by Ibaraki prefecture.

Author Contributions: Conceptualization, Y.N., S.K., T.M. (Tomomi Masui) and H.K.; methodology, Y.N., T.O. and S.K.; data curation and formal analysis, Y.N.; investigation, Y.N., and T.M. (Tomoki Maeda); resources, Y.N., T.M. (Tomoki Maeda), T.O. and T.M. (Tomomi Masui); writing—original draft preparation, Y.N.; writing—review and editing, S.K.; supervision, S.K. and H.K.; project administration, S.K. and H.K. All authors have read and agreed to the published version of the manuscript.

Conflicts of Interest: The authors declare no conflict of interest.

References

1. Abragam, A.; Goldman, M. Principles of dynamic nuclear polarization. *Rep. Prog. Phys.* **1978**, *41*, 395–467. [CrossRef]
2. Niinikoski, T.O. *The Physics of Polarized Targets*; Cambridge University Press: Cambridge, UK, 2020; pp. 155–198.
3. Bunyatova, E.I. Free radicals and polarized target. *Nucl. Instr. Meth. Phys. Res. A* **2004**, *526*, 22–27. [CrossRef]

4.	Noda, Y.; Kumada, T.; Hashimoto, T.; Koizumi, S. Small-angle neutron scattering study of dynamically polarized polyethylenes. *Physica B* **2009**, *404*, 2572–2574. [CrossRef]

5.	Noda, Y.; Kumada, T.; Hashimoto, T.; Koizumi, S. Inhomogeneous dynamic nuclear polarization of protons in a lamella-forming diblock copolymer investigated by a small-angle neutron scattering method. *J. Appl. Cryst.* **2011**, *44*, 503–513. [CrossRef]

6.	Noda, Y.; Koizumi, S.; Masui, T.; Mashita, R.; Kishimoto, H.; Yamaguchi, D.; Kumada, T.; Takata, S.; Ohishi, K.; Suzuki, J. Contrast variation by dynamic nuclear polarization and time-of-flight small-angle neutron scattering. I. Application to industrial multi-component nanocomposites. *J. Appl. Cryst.* **2016**, *49*, 2036–2045. [CrossRef] [PubMed]

7.	Stuhrmann, H.B.; Schärpf, O.; Krumpolc, M.; Niinikoski, T.O.; Rieubland, M.; Rijllart, A. Dynamic nuclear polarisation of biological matter. *Eur. Biophys. J.* **1986**, *14*, 1–6. [CrossRef] [PubMed]

8.	Masuda, Y. Neutron scattering by inhomogeneous distribution of proton polarization produced by the dynamic nuclear polarization. *Hyperfine Interact.* **1987**, *35*, 1071–1074. [CrossRef]

9.	Van den Brandt, B.; Glättli, H.; Grillo, I.; Hautle, P.; Jouve, H.; Kohlbrecher, J.; Konter, J.A.; Leymarie, E.; Mango, S.; May, R.P.; et al. Time-resolved nuclear spin-dependent small-angle neutron scattering from polarized proton domains in deuterated solutions. *Eur. Phys. J. B* **2006**, *49*, 157–165.

10.	Kumada, T.; Noda, Y.; Hashimoto, T.; Koizumi, S. Dynamic nuclear polarization system for the SANS-J-II spectrometer at JAEA. *Physica B* **2009**, *404*, 2637–2639. [CrossRef]

11.	Noda, Y.; Koizumi, S. Dynamic nuclear polarization apparatus for contrast variation neutron scattering experiments on iMATERIA spectrometer at J-PARC. *Nucl. Instr. Meth. Phys. Res. A* **2019**, *923*, 127–133. [CrossRef]

12.	Ishigaki, T.; Hoshikawa, A.; Yonemura, M.; Morishima, T.; Kamiyama, T.; Oishi, R.; Aizawa, K.; Sakuma, T.; Tomota, Y.; Arai, M.; et al. IBARAKI materials design diffractometer (iMATERIA)—Versatile neutron diffractometer at J-PARC. *Nucl. Instr. Meth. Phys. Res. A* **2009**, *600*, 189–191. [CrossRef]

13.	Takada, H.; Haga, K.; Teshigawara, M.; Aso, T.; Meigo, S.; Kogawa, H.; Naoe, T.; Wakui, T.; Ooi, M.; Harada, M.; et al. Materials and Life Science Experimental Facility at the Japan Proton Accelerator Research Complex I: Pulsed Spallation Neutron Source. *Quantum Beam Sci.* **2017**, *1*, 8. [CrossRef]

14.	Nakajima, K.; Kawakita, Y.; Itoh, S.; Abe, J.; Aizawa, K.; Aoki, H.; Endo, H.; Fujita, M.; Funakoshi, K.; Gong, W.; et al. Materials and Life Science Experimental Facility (MLF) at the Japan Proton Accelerator Research Complex II: Neutron Scattering Instruments. *Quantum Beam Sci.* **2017**, *1*, 9. [CrossRef]

15.	Sakasai, K.; Satoh, S.; Seya, T.; Nakamura, T.; Toh, K.; Yamagishi, H.; Soyama, K.; Yamazaki, D.; Maruyama, R.; Oku, T.; et al. Materials and Life Science Experimental Facility at the Japan Proton Accelerator Research Complex III: Neutron Devices and Computational and Sample Environments. *Quantum Beam Sci.* **2017**, *1*, 10. [CrossRef]

16.	International Commission on Non-Ionizing Radiation Protection. Guidelines on limits of exposure to static magnetic field. *Health Phys.* **2009**, *96*, 504–514. [CrossRef] [PubMed]

17.	Shinohara, T.; Suzuki, J.; Oku, T.; Takata, S.; Kira, H.; Suzuya, K.; Aizawa, K.; Arai, M.; Otomo, T.; Sugiyama, M. Design of a neutron polarizer using polarizing super mirror for the TOF-SANS instrument at the J-PARC. *Physica B* **2009**, *404*, 2640–2642. [CrossRef]

18.	Shinohara, T.; Hiroi, K.; Su, Y.; Kai, T.; Nakatani, T.; Oikawa, K.; Segawa, M.; Hayashida, H.; Parker, J.D.; Matsumoto, Y.; et al. Polarization analysis for magnetic field imaging at RADEN in J-PARC/MLF. *Phys. Conf. Ser.* **2017**, *862*, 012025. [CrossRef]

19.	Sears, V.F. Neutron scattering lengths and cross sections. *Neutron News* **1992**, *3*, 26–37.

20.	Shibayama, M.; Nagao, M.; Okabe, S.; Karino, T. Evaluation of incoherent neutron scattering from softmatter. *J. Phys. Soc. Jpn.* **2005**, *74*, 2728–2736. [CrossRef]

21.	Glättli, H.; Goldman, M. 21. Nuclear Magnetism. *Methods Exp. Phys.* **1987**, *23C*, 241–286.